5550–5562 *Nucleic Acids Research, 2019, Vol. 47, No. 11* *Published online 20 May 2019*
doi: 10.1093/nar/gkz377

A multiscale analysis of DNA phase separation: from atomistic to mesoscale level

Tiedong Sun[1], Alexander Mirzoev[1], Vishal Minhas[1], Nikolay Korolev[1], Alexander P. Lyubartsev[2,*] and Lars Nordenskiöld[1,*]

[1]School of Biological Sciences, Nanyang Technological University, Singapore 637551 and [2]Department of Materials and Environmental Chemistry, Stockholm University, 10691 Stockholm, Sweden

Received February 11, 2019; Revised April 26, 2019; Editorial Decision April 29, 2019; Accepted May 09, 2019

ABSTRACT

DNA condensation and phase separation is of utmost importance for DNA packing *in vivo* with important applications in medicine, biotechnology and polymer physics. The presence of hexagonally ordered DNA is observed in virus capsids, sperm heads and in dinoflagellates. Rigorous modelling of this process in all-atom MD simulations is presently difficult to achieve due to size and time scale limitations. We used a hierarchical approach for systematic multiscale coarse-grained (CG) simulations of DNA phase separation induced by the three-valent cobalt(III)-hexammine ($CoHex^{3+}$). Solvent-mediated effective potentials for a CG model of DNA were extracted from all-atom MD simulations. Simulations of several hundred 100-bp-long CG DNA oligonucleotides in the presence of explicit $CoHex^{3+}$ ions demonstrated aggregation to a liquid crystalline hexagonally ordered phase. Following further coarse-graining and extraction of effective potentials, we conducted modelling at mesoscale level. In agreement with electron microscopy observations, simulations of an 10.2-kb-long DNA molecule showed phase separation to either a toroid or a fibre with distinct hexagonal DNA packing. The mechanism of toroid formation is analysed in detail. The approach used here is based only on the underlying all-atom force field and uses no adjustable parameters and may be generalised to modelling chromatin up to chromosome size.

INTRODUCTION

The compaction of DNA is a problem of outstanding importance in biology with many important applications in polyelectrolyte theory, biotechnology, nanoscience (1–4). While a long (∼100 Mb) chromosomal DNA molecule in low salt solution would adopt a random coil conformation expanding over 100 μm, 46 such DNA molecules are packed inside the confined space of about 10 μm in the human cell nucleus. Similarly, in sperm heads, viruses and bacteria, DNA is extremely densely condensed (4–7). The packaging of the giant genomes of dinoflagellates is another example of compact ordered liquid-crystalline form of DNA (8,9). Notably, in the eukaryotic cell nucleus formation of heterochromatin has recently been proposed to proceed through liquid-liquid phase separation of condensed DNA domains (10,11). DNA condensation has also attracted great attention in gene delivery where the compaction is a key to optimising DNA transfer (3,12).

For almost 50 years it has been known that *in vitro*, in the presence of highly charged cations like cobalt(III)-hexammine ($CoHex^{3+}$), spermidine^{3+} and spermine^{4+}, DNA in solution condenses into collapsed structures of varying morphologies such as toroids, rod like fibres, globules and liquid crystals (13–17). While liquid crystalline phases are observed for 150 bp or shorter DNA molecules (18–20), long DNA molecules (a few to several hundred kbp) exhibit highly regular toroidal structures with DNA arranged in hexagonal packing inside the toroids (6), which have an outer diameter of around 100 nm, depending on conditions (21,22). This spontaneous formation of DNA toroids in hexagonal arrangement is also observed *in vivo* in viruses and sperm chromatin and has fascinated scientists for a long time (5,6,23,24). This phenomenon has been vastly studied experimentally with a variety of techniques such as X-ray diffraction (25), Cryo-EM (22,24) and more recently with single molecule techniques (26). This has resulted in significant advances in our understanding of the phenomenon both at mechanistic and fundamental level. However, there are still many unsolved problems related to the condensation of DNA induced by multivalent cations resulting in the formation of the ordered DNA liquid crystalline phase, and the collapse of DNA into toroidal struc-

*To whom correspondence should be addressed. Tel: +65 6592 75 06; Email: larsnor@ntu.edu.sg
Correspondence may also be addressed to Alexander P. Lyubartsev. Tel: +46 8 16 11 93; Email: alexander.lyubartsev@mmk.su.se
Present address: Tiedong Sun, Department of Materials Science and Chemistry, Institute of High Performance Computing, Agency for Science, Technology and Research (A*STAR), Singapore 138632.

tures. There is a lack of rigorous theoretical modelling approaches that are able to predict, reproduce and analyse these phenomena from basic principles.

Although it may seem counterintuitive, the fundamental origin of multivalent ion induced attraction between like-charged DNA molecules leading to condensation is grounded in the electrostatic properties of the highly charged DNA polyelectrolyte. Based on computer simulations as well as on analytical theories, it has been established that the attraction is caused mainly by ion-ion correlations that result in a correlated fluctuation in the instantaneous positions of the condensed counterions on DNA, leading to a net attractive force between DNA molecules (reviewed in (2,27)). In the case of flexible multivalent cations like the polyamines or oligopeptides, the attraction is also generated by the 'bridging' effect (28). The origin of multivalent ion induced attraction between aligned DNA-DNA molecules is therefore clear and well described by such polyelectrolyte models, and recently also in all-atom detail (29,30). However, the mesoscale level spontaneous transition of short DNA molecules to a hexagonal liquid crystalline phase and the formation of toroids from kbp-long DNA molecules, have not been rigorously described and analysed theoretically. These phenomena that are determined by a combination of electrostatic forces and by DNA mechanical properties, are highly important for understanding DNA phase separation in biology.

Computer modelling of DNA condensation to an ordered bundled phase or modelling of single DNA molecule collapse to the toroid structure, have with few exceptions been performed with a description of DNA as a chain of beads using parameterised harmonic bonds. The bending flexibility was commonly tuned to reproduce the DNA mechanical properties from persistence length data (31–34). Furthermore, the DNA-DNA attraction was generally modelled by empirical potentials. Only in a few of these works electrostatic effects were treated directly by including explicit balancing counterions, however, without added salt (31–33). Common to all these approaches is that they treat generic polymer molecules without explicit presence of added salt, using empirical adjustable parameters to describe the relevant potentials in the models. Hence, the connection to the atomistic DNA structure and chemical specificity is lost. The experimentally important phenomenon of the formation of hexagonally ordered liquid crystalline phase of short DNA molecules in the presence of multivalent counterions has to the best of our knowledge never been theoretically demonstrated.

In recent years advances in computer technology have progressed considerably and all-atom biomolecular MD simulations including molecular water can now be performed for very large systems such as a nucleosome core particle and large DNA assemblies (30,35). Yoo and Aksimentiev developed improved ion-phosphate interaction force field parameters and performed all-atom MD simulations of an array of 64 parallel duplex DNA. They demonstrated the correct hexagonal packing of DNA, which was absent in simulation with standard CHARMM or AMBER force field parameters (36). The same authors also investigated the physical mechanism of multivalent ion-mediated DNA condensation at atomistic level. The results supported a model of condensation driven by entropy gain due to release of monovalent ions and by bridging cations (30).

However, all-atom MD simulation of DNA liquid crystalline formation or kb-size DNA toroid condensation is presently not computationally feasible and hence multiscale approaches linking atomistic and coarse-grained (CG) levels of description are necessary (37). Within a systematic bottom-up multiscale modelling scheme, the macromolecules are reduced to a CG description with effective sites representing groups of atoms and a number of such coarse-graining methods and models for DNA have been developed, each with respective strengths and weaknesses (38).

Some bottom-up approaches, have recently been used to model DNA (39–42) and various DNA properties (flexibility, topological effects, interaction with proteins, DNA aggregation (43–45); see also reviews (37,46)). Most of the reported studies did not treat both electrostatics and solvent effects rigorously, i.e. did not use explicit ion models, or did not study the mesoscopic scale of DNA condensation. An alternative to systematic bottom-up CG approach for modelling DNA at mesoscale level is represented by recent work by the de Pablo group using a top-down approach to fit the model parameters to experimental data (DNA thermal denaturation) (41,47). The DNA model combined with explicit ions was used in simulations of 4 kbp DNA packaging in the presence of multivalent ions inside a virus capsid (48).

The DNA condensation to a hexagonally ordered phase as well as DNA toroid formation, both induced by the presence of multivalent cations, are phenomena clearly intrinsic to the DNA molecule and inherent in its physico-chemical properties. We hypothesise that this behaviour can be predicted by a bottom-up approach that is based on state-of-the-art all-atom molecular dynamics (MD) simulations, which is followed by structure-based coarse-graining resulting in effective interaction potentials for the CG model without further adjustable parameters.

Here, we perform systematic multiscale structure-based CG simulations of DNA with explicit electrostatic interactions included, starting from all-atom description going up to mesoscale modelling of DNA. The CG model is simple enough yet captures the structure form of double helix DNA and rigorously treats the electrostatic interactions. The systematic coarse-graining follows the Inverse Monte Carlo (IMC) approach to extract solvent mediated effective CG potentials for all interactions in the system (49,50) from structural properties of the underlying system. The model is validated in CG simulations of DNA persistence length as a function of monovalent salt demonstrating outstanding performance. We show DNA condensation induced by the three-valent $CoHex^{3+}$ ion for short DNA duplexes resulting in a bundled phase with hexagonal ordering. Furthermore, adopting a second level 'super coarse-grained' (SCG) DNA beads-on-a-string model we show that this approach remarkably predicts the hexagonally ordered liquid crystalline-like phase of short DNA and toroid formation in hexagonal arrangement for kbp-size long DNA, giving mechanistic insight on the DNA condensation process. In order to pave the ground for detailed analysis of the compaction of DNA at mesoscale level in chromosomes, it is necessary to develop similarly chemically informed

bottom-up models for the amino acids modelling histone proteins. Such models should have the predictive power to be trusted in modelling biologically important phenomena at mesoscale level for experimentally unexplored scenarios. The present approach represents a first and successful step in this direction.

MATERIALS AND METHODS

More details on computational methods and parameters used in this work are given in the Supplementary Methods section of the Supplementary Data (SD).

Hierarchy of DNA models

The hierarchical multiscale approach used here implements systematic stepwise coarse-graining of DNA model from the atomistic to a beads-on-string level as illustrated in Figure 1. Coarse-graining is performed at two spatial scales resulting in three DNA models with different resolutions. Figure 1A illustrates the all-atom DNA model which includes explicit water molecules and ions. In the CG DNA model (Figure 1B), the DNA is modelled with five beads, representing a two-base pair unit of DNA (Figure 1D). There are four types of bonds and three types of angles in the bonded interaction terms (Figure 1D). We include explicit mobile ions and charges of DNA phosphate groups while the solvent is considered implicitly. As detailed below and in the Supplementary Data, for the CG model we have performed three different parameterisations at the CG level, based on three different all-atom systems.

For the CG model, this results in a large number of interactions parameterised, all of them calculated by the IMC procedure except for long-range electrostatics. The exact number of interactions depends on the composition of the CG system. In summary, the CG model includes the following type of interactions: (i) bonded interactions between DNA beads (see Figure 1D), (ii) angle interactions between DNA beads (Figure 1D), (iii) intermolecular short-ranged non-bonded terms between DNA beads, (iv) intermolecular short-ranged non-bonded terms between charged mobile ions as well as between ions and DNA D/P beads, (v) long-range electrostatic interactions, which are the same in all systems and described by Coulombic interactions in a dielectric continuum described by the dielectric permittivity of water, (vi) short-range intramolecular interactions within one DNA molecule (see details in the Supplementary Methods). Supplementary Table S1 summarises all interaction types for the three different CG parameterisations performed (see details below and in the Supplementary Data).

The second level of coarse-graining results in a beads-on-string type of model, called the super CG DNA (SCG) model, which is shown in Figure 1C. Here, a single type of uncharged beads (called 'S') represents three units of the CG DNA model, corresponding to six DNA base pairs. There is one bond and one angle potential as well as the presence of non-bonded intermolecular and intramolecular effective potentials between the S beads, which are parameterised by IMC. In the SCG model both solvent and electrostatic interactions are implicitly included into the effective potentials (see details below).

It may also be noted that the geometry and topology of the CG model preserves the DNA chirality. However, this model would also be applicable to a left-handed helix, but under the present conditions, the structure is constrained to the initial right-handed form due to the large conversion barrier. The DNA in the SCG model does not have chirality.

All-atom molecular dynamics simulations

Three different all-atom simulation corresponding to set-up of the given all-atom system are set up. These correspond to the three parameterisations made within the IMC procedure (see details below).

First, we perform all-atom MD simulations of a single 40 bp DNA in the presence of 130 mM NaCl. This is used in IMC parameterisations for validation of experimental behaviour of persistence length as a function of ionic strength.

Second, simulations in the presence of $CoHex^{3+}$ ions, which induces condensation of DNA to fibres are performed. Here, three independent microsecond-long all-atom MD simulations are performed with four 36 bp-long DNA molecules (the sequences are given in the SD) in presence of water and ions as illustrated in Figure 2. The system contains $CoHex^{3+}$ ions corresponding to 1.5 times the charge of the DNA. Additionally the system contains added salt corresponding to 50 mM K^+ and 35 mM Na^+, with neutralising amount of Cl^- ions.

Third, a similar setup as case two above, but with the $CoHex^{3+}$ ions replaced by Mg^{2+} is made. This serves as a control simulation performed to demonstrate absence of DNA–DNA attraction and no DNA condensation in all-atom and in CG simulations in the presence of Mg^{2+} as observed in experiments.

The CHARMM27 force field is used in all simulations, supplemented with Car-Parrinello MD (CPMD) optimised $CoHex^{3+}$ parameters obtained in our previous work (51).

Inverse Monte Carlo procedure

In both the CG and SCG DNA models, all effective interaction potentials are obtained in a systematic and rigorous way using the IMC method (49,50). The potentials are constructed to reproduce selected average structural properties of the fine-grained system such as radial distributions functions (RDF) between non-bonded CG sites and bond length and angle distributions for bonded sites. For the CG DNA model, these are obtained by mapping the all-atom MD trajectory from the four-DNA system to a corresponding CG site representation. Thus, no empirical or adjustable parameters are used in the CG DNA model and it rests only on the parameters from all-atom CHARMM27 DNA and ions as well as on the CPMD optimised parameters for $CoHex^{3+}$. The IMC-derived potentials are tabulated and not prescribed by any specific functional form.

The topology of the CG DNA model (Figure 1B and D) is similar to our previous CG DNA model (52,53). But the current CG DNA model has all its interaction potentials derived by the IMC method from the underlying atomistic simulations. The total number of bead types is nine: four DNA beads (D, P, as well as terminal DT, PT), one $CoHex^{3+}$, one Mg^{2+}, one K^+, one Na^+ and one Cl^- bead.

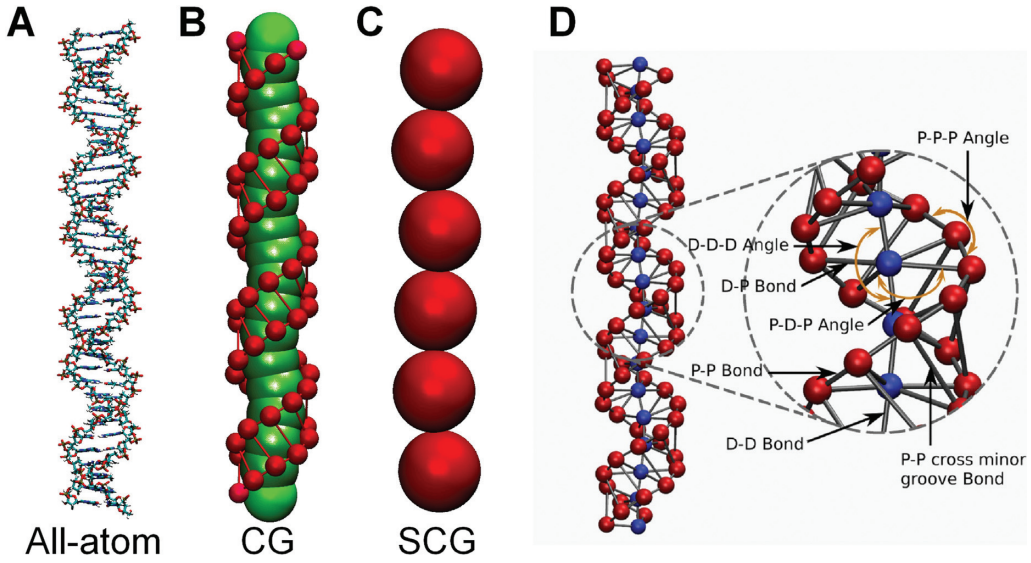

Figure 1. Hierarchy of DNA models. (**A**) The all-atom DNA model. (**B**) The first level of DNA coarse-graining with two bead types. (**C**) The SCG model is built upon the CG model with one bead type. (**D**) The detailed presentation of the CG DNA model in (**B**). Bond interactions, D–P, P–P (backbone), D–D and P–P (cross minor groove) are shown in grey. Angle interactions (P–D–P, P–P–P and D–D–D) are indicated by orange arrows.

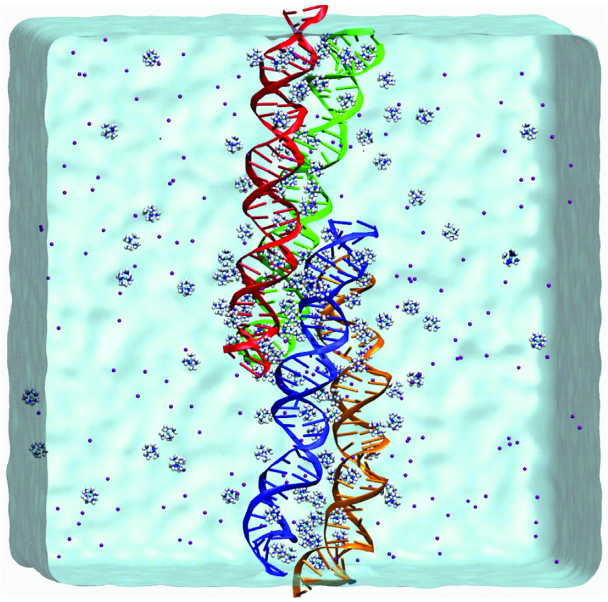

Figure 2. Bundling of DNA in all-atom MD simulations in the presence of $CoHex^{3+}$. A snapshot shows formation of a bundle of the four 36 bp DNA double helices (coloured blue, red, green and orange) in the cubic box of 15 nm size. Ions (140 $CoHex^{3+}$, 140 K^+, 95 Na^+, 375 Cl^-) are shown as spheres and explicit water is displayed as blue surface.

The complete set of interaction parameters consists of 44 non-bonded terms, 4 bonded terms and 3 angle terms (see details in Supplementary Data, Supplementary Table S1). All effective interaction potentials are derived simultaneously, on the basis of atomistic simulation described in the previous section, so that all correlations between different interaction terms are taken into account. It can be noted that the present DNA model is not parameterised for sequence specificity but such an extension is possible by treating each unique two-base pair step individually at the mapping stage (there being 10 unique steps).

The potentials for the SCG model are derived in the same way as for the CG model using the IMC method. Trajectories generated by MD simulation of the CG model are mapped to the SCG representation. Then the RDF between the 'S' sites, as well as bond and angle distributions are calculated with the mapped SCG trajectories. The IMC procedure is subsequently used to derive the potential.

It should be noted that in addition to the short-range part of effective potential (which has cut-off range of 25 Å), all charged sites are interacting by a Coulombic potential (scaled by the dielectric constant). This means that beyond the range of 25 Å, interactions are primarily electrostatic-driven. These long-range interactions are treated using Ewald summation or the Particle-Particle Particle Mesh (PPPM) algorithm. The dielectric constant is set to 78.0. A detailed discussion of this approach is given in (54).

Effective ionic potentials for the same interactions that are obtained from different parameterisations are generally very similar (see below). However, our methodology is structure-based, and it is therefore preferable to make separate parameterisations for systems that display considerably different structural features in experimental behaviour and conditions.

In summary, we have performed three different IMC parameterisations at the CG level, based on three different all-atom systems. At the SCG level, one IMC parameterisation is performed based on the CG MD simulation with $CoHex^{3+}$. General information about simulations at all three scale levels and their computational efficiency (CPU usage time) is given in Supplementary Table S2 in the SD. Supplementary Table S1 lists all the interaction potentials that are calculated in the CG models for the three separate parameterisations that have been performed. All tabulated potentials are provided in the SD in an archive zip file.

The IMC calculation is carried out with the MagiC software v.3 (55) that is also used for bead-mapping, RDF calculation, analysis and export of the resulting potentials.

Coarse-grained simulations

Following the extraction of effective CG potential with the IMC method, we use these potentials to perform CG MD simulations for a system comprising two hundred DNA molecules and explicit ions to simulate DNA aggregation in the presence of $CoHex^{3+}$. The simulation box is constructed with 200 pieces of 100-bp DNA (50 CG-DNA units) in a 150 × 150 × 150 nm^3 simulation box containing 13 200 $CoHex^{3+}$ ions (corresponding to a concentration of 6.5 mM) in the presence of 10 mM K^+ and 10 mM Na^+ ions as well as neutralising Cl^- ions. This simulation is used for further coarse-graining to a 'super-CG' (SCG) DNA model (Figure 1C) with another step of IMC. The derived effective potentials for the SCG model enable us to simulate DNA condensation and phase separation at mesoscale level. We perform simulations with the SCG model for two systems. The first comprises 400 pieces of 96 bp DNA (represented by a chain of 16 S-beads) and the second system is a single 10.2 kb-long DNA (1700 S-beads). Within the SCG model, the electrostatic interactions are treated implicitly since they are effectively included into the SCG effective potentials. The simulations with the CG and SCG DNA models are conducted using the LAMMPS package (56) in the NVT ensemble.

Persistence length calculation

To validate the CG DNA model we test its performance in prediction of the salt dependence of the DNA persistence length, L_p. We perform all-atom MD simulations of a single 40 bp DNA in the presence of physiological salt (130 mM NaCl) (the first simulation in the section **All-atom molecular dynamics simulation**). Following that we make the mapping of this trajectory to the CG model and extract effective IMC potentials. To estimate the dependence of the persistence length on ionic concentration, a 500 bp long CG DNA is simulated in the range of NaCl salt concentrations from 0.1 to 100 mM. Our simulation results are compared with experimental data and with data from other simulation studies.

The persistence length is calculated according to the formula $L_p = -L_c/(\ln(<\cos\alpha>))$. Here, L_c is the contour length of the DNA fragment and $<\cos\alpha>$ is the average of the cosine of the angle between two adjacent DNA segments. The average is taken over the length of the simulation and over the positions of the segments on DNA for the corresponding contour length. Then $(\ln(<\cos\alpha>)$ is plotted as a function of L_c. L_p is estimated by determining the slope of the plot, as done in our previous study (53). We do not determine L_p in atomistic simulations, but in coarse-grained simulations, where the length of DNA (500 bp) is longer than the Kuhn segment.

Physically, the persistence length is defined by the DNA local flexibility and by the long-range interactions which have mostly electrostatic and excluded volume nature. The DNA local flexibility is determined by the bonded interactions of the CG model, which are well parametrised from the atomistic simulations of the 40 bp fragment. The long-range interactions of the CG model consist of a short-range part (within cut-off distance) representing excluded volume and solvent-mediated interactions, which is parameterised from the atomistic simulations, and the electrostatic part which is not limited by distance but strictly treated in the CG simulations by the PPPM method.

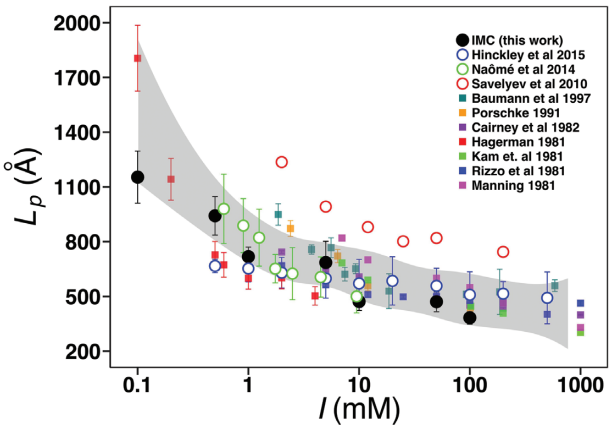

Figure 3. Dependence of DNA persistence length (L_p) on NaCl concentration (I). Solid black circles are data of this work. Solid squares are experimental results: dark cyan (57), orange (58), dark magenta (59), red (60), green (61), blue (62), magenta (63). Hollow circles are results from other computer simulations with explicit ions: blue (41), green (64), red (42). Shaded area is the spline approximation of the experimental data with confidence level 0.99995.

RESULTS AND DISCUSSION

Validation of the CG DNA model and the approach

First we validate the approach and the CG DNA model (described above) against experimental persistence length data as a function of monovalent salt concentration. We perform an all-atom MD simulation of a single 40 bp DNA in the presence of physiological salt (130 mM NaCl). The all-atom trajectory is run for 2 μs and demonstrates stability of helical parameters and the elasticity of the DNA double helix (data not shown). We then extract effective short-range potentials (see Supplementary Methods for details). Supplementary Figure S1 of the Supplementary Data (SD) shows all the effective potentials. Following that, we proceed to run several CG simulations of a single 500 bp-long DNA molecule in the presence of varying concentration of monovalent salt in the range of 0.1–100 mM. Figure 3 compares the dependence of persistence length as a function of salt concentration with experimental data (57–63). We include experimental persistence length data from several sources as there is a large variation in these results depending on the method used and the procedure for analysing the original measurements. Additionally, we also include values predicted by other CG DNA models with explicit ions, obtained using bottom-up approaches based on underlying all-atom MD simulations of single DNA oligonucleotides (41,42,64). Considering the variation in experimental data, the present model demonstrates excellent agreement with experiments for three orders of magnitude variation in salt concentration. However, the results of our model seem to

display somewhat lower L_p values as compared to experiment, which implies that within this model, DNA may be slightly more flexible than real DNA. In general, the performance of our model is superior to other available explicit ion CG DNA models. This accurate prediction of the effect of electrostatic interactions on DNA flexibility lends confidence to the present approach. The result shows that the model well represents both DNA intrinsic flexibility and electrostatic interactions. A more detailed discussion of DNA flexibility and persistence length prediction from the CG model and how the DNA flexibility depends on choice of underlying force field will be presented elsewhere (Minhas *et al*., to be published).

DNA-DNA attraction in all-atom MD simulations

We perform all-atom MD simulations for a system with four DNA molecules containing explicit ions ($CoHex^{3+}$, Na^+, K^+ and Cl^-) and water. A snapshot of the system is shown in Figure 2. Data from the three independent 1 μs-long simulations are subsequently used in the IMC procedure for extraction of effective solvent mediated potentials for the CG DNA model.

Similarly to the result of our previous work (51), the system shows DNA–DNA attraction and aggregation of DNA into fibre-like bundles induced by $CoHex^{3+}$ (Figure 2). DNA fibres are formed across the periodic boundaries in all three independent simulations (see Supplementary Figure S2A–C). The snapshots show some variability in the character of DNA–DNA contacts over the periodic images. In order to obtain rigorous RDFs it is important to analyse an equilibrated ensemble. It is, however, clear that for an all-atom MD simulation of a system of molecules of this size with very strong electrostatic coupling, it cannot be claimed that the system is fully equilibrated. This is the reason why we averaged the RDF from three independent runs. We believe that typical configurations of several local minima sampled in independent simulations can capture the most characteristic configurations of DNA and ions, providing a realistic estimate of the intermolecular interactions. Furthermore, the electrostatics is the main force driving the large scale behaviour of polyelectrolytes such as DNA, while the specific short-range interactions determine details (65). It is therefore not unreasonable to suggest that these short-range specific interactions, which are determined by RDFs obtained from atomistic simulations can be realistically reproduced by sampling configurations within local energy minima. Since CG models generally present a smoother free energy surface than their fine-grained counterpart, more efficient sampling can be achieved in CG MD simulations. It should, however, be noted that the condensed configurations may not represent the lowest free energy state, being constrained by the local minimum.

After extracting the effective potentials for the CG model, longer CG MD simulations of the same system with four DNA molecules, are performed (see more details in the next section). A final snapshot from one CG-MD simulation of this four DNA system is shown in the Supplementary Figure S2D. In the CG MD simulations, a straight fibre configuration is easily reached. This result is stable and does not vary in different simulations. This gives additional confidence for the trust in the effective potentials obtained from the all-atom MD simulation, in spite of the general problem of sampling of the complete configuration space in the all-atom simulations.

Coarse-grained DNA model with rigorous effective solvent mediated potentials

Following the all-atom MD simulations of the system with four DNA molecules in all-atom representation containing explicit ions ($CoHex^{3+}$, Na^+, K^+ and Cl^-) and water as described above, we proceed to extract the effective potentials for the CG model. The trajectories generated by the three atomistic MD simulations are mapped from the all-atom to the CG DNA model. We use these for calculation of RDFs and intramolecular (within DNA) distributions of bond lengths and angles between the CG sites, with averaging over all three independent trajectories. Selected examples of calculated RDFs and distribution functions are shown in Figure 4A–C. Corresponding effective potentials are plotted in Figure 4D–F. All RDFs and effective potentials for the CG DNA model in the presence of $CoHex^{3+}$ can be found in Supplementary Figure S3. All charged sites interact by a Coulombic potential (scaled by the dielectric constant) and treated by the Ewald summation. DNA interacts by this potential beyond 25 Å, which is the cut-off used only for the short-range part of the total potential. It is only the short-ranged parameterised part of the potential that is displayed in Figure 4. Supplementary Figure S4 illustrates convergence in the IMC calculations.

We additionally performed a control all-atom MD simulation without the presence of $CoHex^{3+}$ under conditions that should not lead to DNA condensation. The $CoHex^{3+}$ ions are replaced by the same number of Mg^{2+} ions (with the corresponding decrease in number of Cl^- counterions), resulting in the absence of DNA condensation, which is in agreement with the experimentally known fact that the divalent Mg^{2+} does not induce DNA condensation (1) (data not shown). We follow the same modelling protocol as for the case of $CoHex^{3+}$ to derive effective potentials for this control model.

It may be noted that the D–D RDFs in the Mg^{2+} and $CoHex^{3+}$ systems between the central beads of different DNA molecules (Figure 4A) appear very different. However, the final effective potentials for the D–D pair from both simulations (Figure 4D) have similar features. They are both slightly attractive from ∼21 Å to the cut-off 25 Å. In the distance range below 21 Å, both effective potentials are repulsive. In the Mg^{2+} system, the RDF at distances <25 Å has low amplitude since different DNA fragments repel each other due to electrostatic interactions. The presence of Mg^{2+} counterions cannot overcome this repulsion. In the more strongly coupled $CoHex^{3+}$ system, the presence of the trivalent counterions creates an overall attraction between DNA segments that leads to DNA condensation. Therefore, it is expected that similar D-D potentials result in different D-D RDFs if different ions are present in the system.

Furthermore, the effective potentials for monovalent ion–ion interactions obtained under different conditions are virtually the same as illustrated in Figure 4F for the case of the Na-Cl pair. In Figure 4C the corresponding

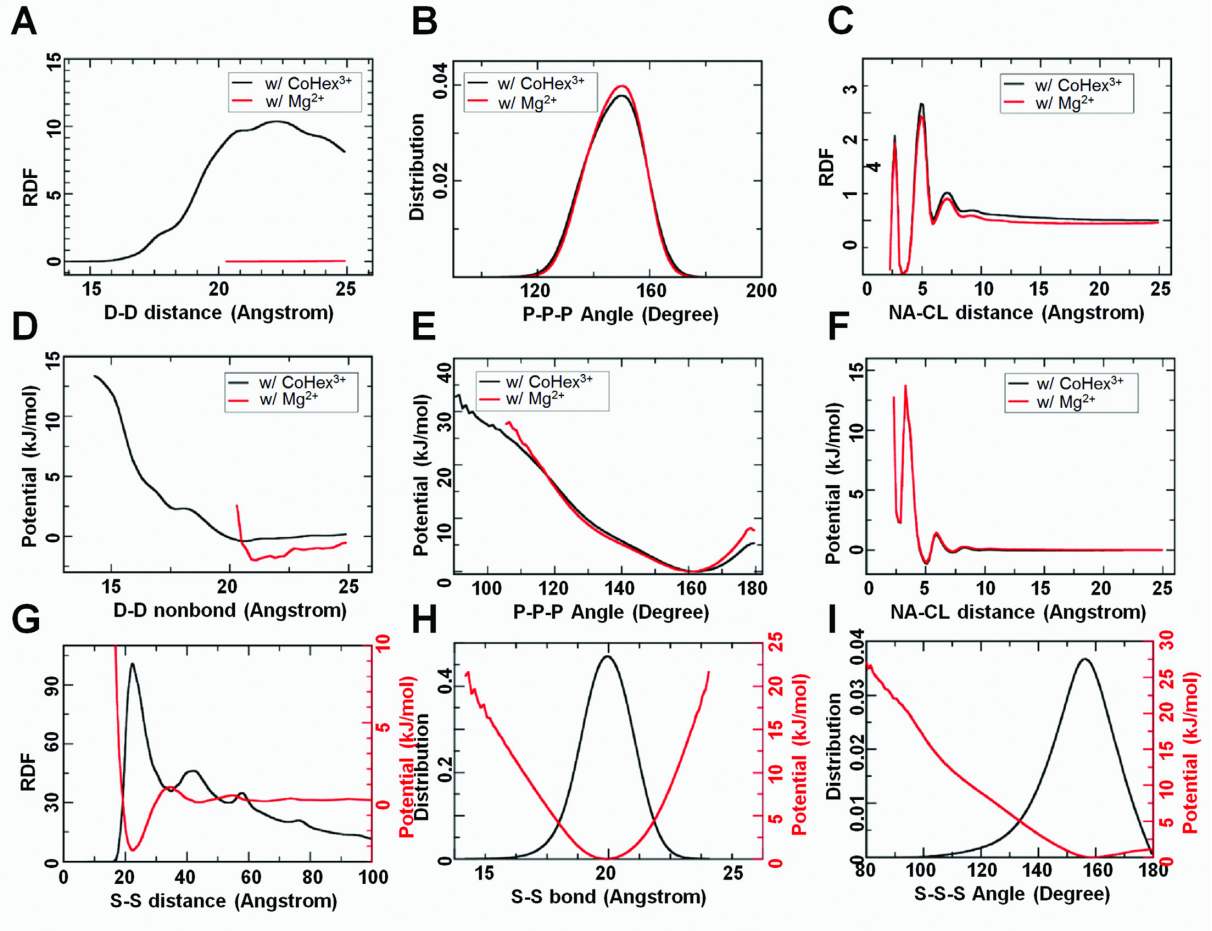

Figure 4. Illustration of RDFs and corresponding effective potentials obtained by the IMC method. Selected RDFs (top row), effective potentials of the CG model (middle row) and all RDFs and effective potentials of the SCG model (bottom row). In (**A–F**), three distributions and corresponding potentials are presented: D–D non-bonded pair, P–P–P angle along backbone and Na–Cl non-bonded pair, from the systems with $CoHex^{3+}$ (black) and Mg^{2+} (red) ions. In (**G–I**), distributions and effective potentials of the SCG model are plotted together for the S–S non-bonded interaction (**G**), the S–S bond (**H**) and the S–S–S angle (**I**).

Na–Cl RDF shows, however, a small but noticeable difference between the aggregating ($CoHex^{3+}$-system) and non-aggregating (Mg^{2+}-system) simulations due to different average DNA–DNA distances. However, the final effective potentials from both systems are identical (Figure 4F). We attribute this to the fact that correlations between the different interaction terms are well captured in the present model. In fact, all ionic potentials for the same interaction types, but extracted from different underlying all-atom MD simulations for the present CG DNA model, are indistinguishable or very similar. As a further illustration, Supplementary Figure S5 compares ionic potentials extracted from three DNA all-atom MD simulations having different ionic and different DNA compositions. This behaviour implies good transferability of the derived potentials (see below for further discussion).

DNA condensation in CG simulations

Having rigorously extracted effective potentials for the CG DNA model on the basis of the all-atom simulations, we next proceed to use them in large-scale simulations investigating DNA phase separation induced by the presence of explicit $CoHex^{3+}$ ions. The applied CG approach treats long-range electrostatic interactions explicitly with the presence of all mobile ions in the system. The total solvent-mediated interaction potential between all charged sites in the system is a sum of a Coulombic potential scaled by the dielectric permittivity of water ($\varepsilon = 78$), and a short-range non-bonded interaction (shown in the figures, e.g. Figure 4) within the cut-off distance, determined by the IMC procedure. This treatment of the long-range electrostatic interactions was validated in our previous work (54). Not only does this lead to a rigorous description of the important electrostatic interactions, but also enables the CG model to be used under varying ionic conditions. It is therefore possible to run CG simulations for other ion compositions and concentrations without having to rerun atomistic simulations. This means that in future studies, we can address salt dependent effects within the CG model. It may be noted that the SCG model (below) is not transferable as it does not include explicit ions. For other salt conditions, the effective potentials in the SCG model would need to be recalculated. This can be done within the CG model where we can easily change

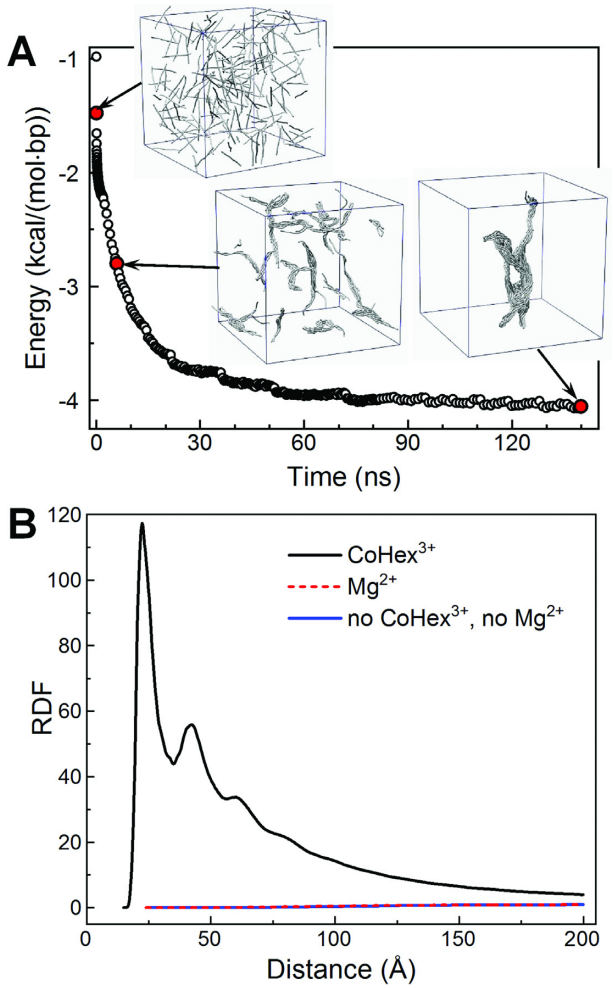

Figure 5. Illustration of DNA phase separation in CG simulations. (**A**) Snapshots and short-range interaction energy profile from the CG DNA simulation. Time points corresponding to each snapshot are indicated with red circles on the energy curve. DNA molecules are drawn as gray tubes following the path of the double helix; mobile ions are not shown. (**B**) Comparison of the D–D RDF determined in the CG simulations with the $CoHex^{3+}$ (black), Mg^{2+} (red dashed) ions and with monovalent salt (blue).

the ion composition since all electrostatics is explicit, while DNA-DNA potentials can, with a good confidence, be considered as independent of the salt content. So, this two-step procedure is also practical if one wishes to generate SCG models for different ion conditions.

After the significant reduction in the number of degrees of freedom by the coarse-graining, we can easily simulate DNA condensation in a box of size of 150 × 150 × 150 nm^3 for extended time. This is 1000 times larger volume compared to what is affordable for the all-atom MD simulations, which have used a box of 15 × 15 × 15 nm^3. Here, 200 pieces of 100-bp CG DNA double helices are randomly placed in the box together with $CoHex^{3+}$, potassium and sodium ions as well as the appropriate amount of chloride ions.

Figure 5A displays the short-range energy of the CG model as a function of time with representative snapshots and illustrates that DNA aggregation and phase separation occurs gradually during the simulation. The DNA condensate particle gets larger, forming a single fibre-like particle at the end of the simulation. Interestingly, the DNA molecules demonstrate short-ranged local order of hexagonal arrangement in the fibre bundle. This illustrates that the almost universal hexagonal packing of condensed DNA is intrinsically inherent in the chemical and physical properties of the DNA molecule as represented by the underlying all-atom force field and preserved in the effective potentials.

The value of the shortest DNA–DNA distance is r = 22.5 Å, as it is exhibited by the first peak of the RDF in Figure 5B. This is in reasonable agreement with experimental data. Our own observations (unpublished data) from X-ray diffraction measurements of precipitated 177 bp DNA molecules, display a single broad Bragg peak at $q = 0.26$ $Å^{-1}$. This corresponds to a lateral DNA-DNA separation in the range 24–27 Å (assuming hexagonal ($r = 4\pi/q\sqrt{3}$) or lamellar ($r = 2\pi/q$) packing). A shorter separation observed for bundled DNA in simulations compared to experiment is likely due to the CHARMM force field presently used in the underlying all-atom MD simulations (66).

To demonstrate the robustness of the CG DNA model, we conduct another simulation where the $CoHex^{3+}$ ions are replaced by K^+ and Na^+ ions with equivalent amount of charge, using potentials obtained from the IMC procedure described above. The same CG box size and simulation protocol are adopted. The system exhibits no DNA condensation and the DNA-DNA interaction is repulsive as can be seen from the D–D RDF plotted in Figure 5B (blue line). In contrast to the system with $CoHex^{3+}$, the amplitude of the D–D RDF is low in value, suggesting a large distance between DNA molecules. Additionally, Figure 5B displays the D–D RDF (dashed red line) obtained from a CG simulation where the $CoHex^{3+}$ ions are replaced by Mg^{2+} ions, with all potentials obtained from the all-atom system comprising four DNA molecules and Mg^{2+} ions, as mentioned above in relation to Figure 4D–F. In agreement with the experimental data (1), this system is repulsive and phase separation does not occur. Hence, we can conclude that our CG DNA model is robust and produces realistic DNA aggregation behaviour in large-scale simulations in agreement with experiment.

The result illustrated in Figure 5B also lends support for the transferability of the effective ionic potentials obtained with the present approach. The CG simulation resulting in the repulsive D–D RDF (red line in Figure 5B) is performed for a system with 200 DNA molecules of 100 bp length containing only monovalent ions. In such a system the expected macroscopic behaviour is that DNA condensation should not occur. However, the effective ionic potentials used in the CG simulation resulting in this non-aggregating system are obtained from an all-atom MD simulation containing $CoHex^{3+}$ ions that displays aggregation and bundling at all-atom level (Figure 2). As a further test of the transferability of the ionic potentials, we compare effective potentials for all monovalent ion interactions obtained by the IMC procedure from two different underlying all-atom MD simulations, displayed and discussed in Supplementary Figure S5. An additional test of transferability is illustrated in Supplementary Figure S6.

Mesoscopic-scale simulations of DNA hexagonal phase separation

To investigate DNA phase separation at the mesoscopic level we perform one more step of coarse-graining, constructing the super coarse-grained (SCG) model. The excellent behaviour of the CG DNA model allows us to confidently build a DNA model with even lower resolution and better performance in terms of simulated time scale. The ions, as well as all electrostatic interactions are treated implicitly by the effective potentials. RDFs and effective potentials comprising the SCG DNA model are illustrated in Figure 4G–I. Due to the simplicity of the model there is no significant correlation among the three interaction terms; the bond and angle potential minima are at the same position as the maxima in the corresponding respective distributions. These two terms may in principle be modelled by simple harmonic functions. On the other hand, the non-bonded interaction term cannot be directly fitted by conventional functions, such as a Lennard–Jones or Debye–Hückel potentials. Specifically, although there is a dominant minimum at 23 Å in the non-bonded effective potential, which might be mimicked by a Lennard–Jones potential, the long-range behaviour of the IMC-computed potential is different, with a positive maximum at 35 Å followed by two relatively small minima at about 44 Å and 65 Å. Hence, the final effective potential contains interaction features that preserve the characteristics of the underlying fine-grained CG simulation as well as the all-atom MD simulation. The present systematic hierarchical multiscale modelling approach can thus preserve more detailed information even with a DNA representation as simple as beads-on-a-string.

The resulting SCG DNA model is used in mesoscale simulations of DNA phase separation for two types of systems. First, 400 relatively short DNA molecules, each one equivalent to 96 bp, are randomly placed in a $150 \times 150 \times 150$ nm^3 box. At the end of this simulation, DNA condense into large particles consisting of >100 DNA molecules as illustrated in Figure 6A. Noticeably, inside these aggregates, DNA molecules are arranged in such a way that the hexagonal structure can be seen from the cross-section of the particle (illustrated in the cross-section view in Figure 6B), in agreement with experimental data obtained for short DNA molecules in the presence of the trivalent cations, $CoHex^{3+}$ and $spermidine^{3+}$ (18,19).

Secondly, we perform simulations for a single 10.2 kb long DNA molecule with the SCG DNA model. The simulations start from a fully extended DNA conformation. After a short relaxation at the beginning, a loop or a bundle can form at either end of the DNA (see Supplementary Movie S1). The top snapshot in Figure 6C shows the DNA conformation after such a loop formation. Subsequently, the loop and bundle play the role of nucleation sites, attracting more DNA beads to form a toroid that grows in size (see Supplementary Movie S2). Towards the end of the simulation, the whole DNA molecule is condensed into one toroidal particle (see Supplementary Movie S3). The non-bonded interaction energy decreases as the toroid grows in size, illustrated by the energy profile in Figure 6C. Remarkably, as can be seen in Figure 6D, the cross section of the toroid shows that DNA is organised in well-defined hexagonal arrangement. These structural features are consistent with the reported electron microscopy studies (6).

Analysis of multiple simulations of single 10.2 kb long DNA molecules reveals that toroids are mainly formed in two ways. The first scenario suggests that a single loop at one end initiates the toroid formation, while the other end may eventually form a fibre that subsequently joins the toroid at the end of the simulation (see Supplementary movies S1–S3). Secondly, a loop may get formed at each end in the beginning of the simulation with the simultaneous growth of two toroids that eventually join together (exemplified in Supplementary movie S4). An interesting feature of DNA toroid formation and size increase, is the sliding motion between contacting DNA segments. DNA toroids can adjust their conformation through this motion simultaneously with the growth due to rolling and attracting more DNA fragments. It should be noted that not only toroids are formed, but the final condensed structure can be fibre-like, which has also been observed in EM experiments (22). In the simulations, the toroid shape is, however, somewhat more frequently occurring. We also simulate a lambda-DNA size single DNA molecules (48 kb) that also form toroids by the mechanism with nucleation loops at both ends (data not shown).

Next we perform an analysis of the mechanism of DNA condensation that results in toroid or fibre bundle formation. We pay specific attention to the pathways and the initial events during DNA condensation that leads to formation of the major final states of toroid or fibre-like morphologies. To this end we perform 67 independent SCG simulations of the 10.2 kbp DNA (having same initial coordinates but with different starting velocities). Although the mechanism of DNA condensation to either toroid or fibre is complex and stochastic, it is possible to identify several intermediate states as well as transitions between them. The formation of either toroid or fibre can be divided into two stages. The first stage can be characterised as nucleation. The second stage includes the growth of the nucleation site that occurs by pulling in more and more DNA chains, and by the sliding mechanism mentioned above. Figure 7 summarises the early event intermediate states and transitions between them. Supplementary Table S3 gives a description of those frequent initial transient structures. In the first few nanoseconds of each simulation, several transient states can be observed, such as state **b** and state **k** in the figure. These are usually simple structures with short lifetimes. As the simulation proceeds, more stable structures can be formed, for example, bundles consisting of three DNA chains (state **c** in the figure) and the double DNA chain loop (state **g**). Based on these more stable structures, the 'growth' mechanism can be effective with the remaining part of the DNA chain being pulled in to form larger and more stable structures.

In the early stage of the simulation, fibre-like structures and toroid-like structures can convert between each other. These structures are usually no more than three DNA chains thick. Hence, the energy barrier involved in these transitions should not be prohibitive. For example, a three DNA chain bundle (state **c**) can convert to a single DNA chain loop (state **h**) to form a toroid-like structure (state **i**). On the other hand, this toroid-like structure (state **i**) is soft

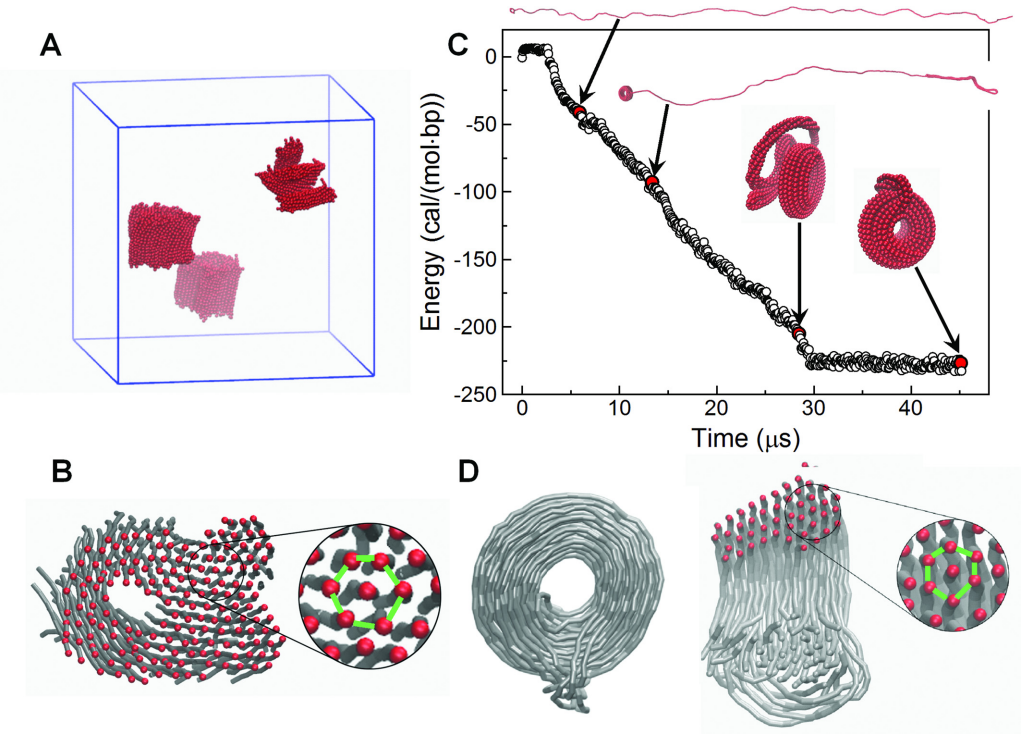

Figure 6. DNA aggregation and toroid formation simulated by the SCG DNA model. (**A**) Final configuration of DNA aggregation in a simulation with 400 DNA molecules. (**B**) Cross-section of one of the DNA condensed particle shown in (A). (C, D) Formation of toroidal structure in the SCG simulations of a 10.2 kb DNA. (**C**) Energy profile and snapshots (normalised per DNA base pair) from one of the simulations. (**D**) Structure of the DNA toroid. Cartoon on the right-hand side shows cross-section through the toroid where the red dots illustrate DNA double helices near the cutting plane. The zoom-in illustrated in (B) and (D) show the DNA packing within the aggregates with green lines highlighting hexagonal arrangement of the DNA molecules.

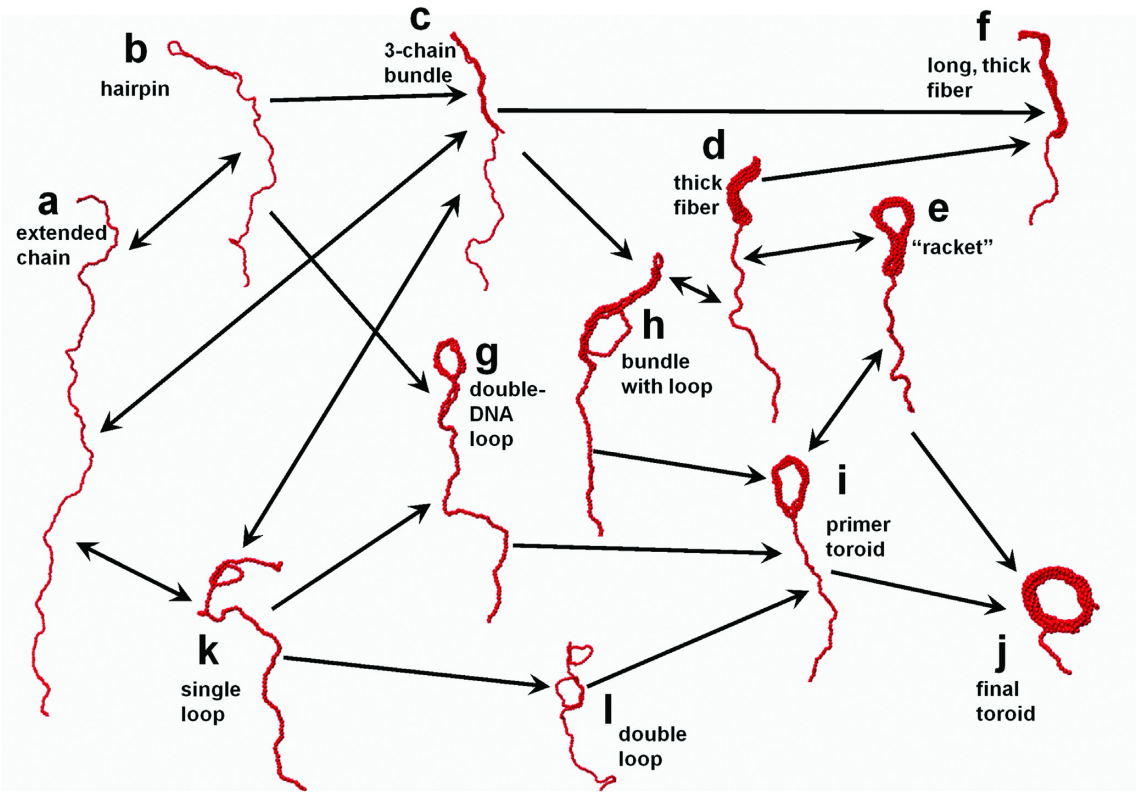

Figure 7. Pathways and intermediate states during formation of DNA toroid and fibre. The structural features of each state are described in more details in Supplementary Table S3. Arrows indicate the transition directions among the states, as observed in the SCG simulations.

enough, so that it can go to a bundle (state **d**) just by closing the hole in the middle. These transitions between fibre-like and toroid-like states rarely happen in the subsequent stages of the simulation when more DNA chains become condensed.

We measure the dimensions of toroids formed by the 10 kb DNA in multiple simulations shown in Supplementary Figure S7. The details of the calculations are given in Supplementary Figure S8. In brief, the projected toroid density map was measured using two circles, one to fit the outer perimeter of the toroid and one to fit the hole. The toroid diameter is an arithmetic average of the diameters of the two circles. Toroid thickness is the difference of the radii of the two circles (see Supplementary Figure S7). The average thickness of the toroid is about 12 nm, which is smaller than in experiments with 3 kbp DNA (∼25 nm) (22). Similarly, the observed diameter (∼22 nm) and hole diameters (∼10 nm) are also smaller than the dimensions observed in the experiments (22). These values are reasonable given the differences between experiments and simulations. The reason for smaller diameter and thickness obtained in simulations comparing to the experiments, might be due to the fact that the simulations contain only a single DNA molecule. Experimentally the toroids formed from DNA of sizes below 50 kb contain several DNA molecules that leads to larger and thicker toroids (22). On the other hand, the diameter of the hole is expected to depend on nucleation loop size mechanism of toroid formation (22) and on the DNA bending properties as well as on effective DNA–DNA attraction. The small hole diameter observed in the simulations is most certainly caused by the intrinsic properties of the underlying force field, which compared to real DNA may represent a mechanically more flexible DNA with stronger attraction leading to shorter DNA–DNA distances and tighter packing in the toroid. The fact that toroid dimensions are strongly affected by electrostatic interactions between DNA molecules was earlier shown by Hud and co-workers (21), who demonstrated a pronounced dependence of toroid diameter and thickness on ionic conditions.

CONCLUSIONS

In conclusion, we have used a rigorous hierarchical multiscale simulation scheme, which enables simulation of DNA condensation at mesoscale levels. The phenomenon of DNA condensation induced by multivalent ions is clearly inherent in the chemical properties of the DNA molecule. Inspired by this fact, we reasoned that a chemically based starting point, using state-of-the-art molecular force fields for all-atom MD simulations, followed by systematic coarse-graining, and using the IMC approach to extract solvent mediated effective CG potentials, would preserve those features of DNA in the CG models. Indeed, DNA condensation induced by the three-valent cobalt(III)-hexammine ions was demonstrated in large-scale simulations of hundreds of DNA molecules, which exhibited correct experimental structural features. We used a hierarchical approach where the CG model was further coarse-grained to a 'super CG' model. Simulations at mesoscale level (10.2 kb DNA) demonstrated toroid formation into hexagonally packed DNA, with reasonable dimensions in qualitative agreement with experimental observations. These results were obtained without any other underlying assumptions except for the all-atom force field and the DNA topology model adopted in the CG simulations and used no adjustable parameters.

The present parameterisation of the CG DNA model is not sequence specific, although this can in principle be introduced at the two-bp step level in the mapping of the all atom simulations. This would however, considerably increase the dimensionality of the CG as all 10 possible unique two-bp steps would have to be parameterised individually and described by separate effective potentials in the IMC procedure. Here we consider a general DNA sequence with mixed AT/GC content close to 50% in the 4-DNA all-atom simulations and 42% GC in the single DNA all-atom simulations. We compare with generic experiments on salt dependence of DNA persistence length and DNA condensation where DNA sequence specificity has generally not been considered. Hence, this approximation is justified. But it should be mentioned that various DNA breathing and bubbling events (bp unpairing) can happen and are allowed in the all-atom simulations and will then be translated to the effective potentials, which in turn means such events are taken into account in the CG model in an average way and would affect the persistence length. Based on our analysis, the frequency of these are force field dependent but effects on the persistence length are minor (Minhas *et al.*, to be published).

In the present work, we used all-atom MD simulations based on the CHARMM27 force field. However, we recently demonstrated similar behaviour in all-atom simulations that showed DNA-DNA attraction and bundling using both CHARMM36 and AMBER parameters (51). It should furthermore be of interest to investigate how the mesoscale simulation results depend on the CG topology comparing different CG DNA models, which include DNA sequence specificity (37,47). It may be noted that the present CG DNA model is not sequence specific, but such an extension can be implemented in our model (53).

The present successful approach lends support for developing CG models for more complicated systems exhibiting DNA compaction at mesoscale level such as chromatin and individual chromosomes. Such models will help understanding the compaction behaviour of chromatin as a function of various variables known to regulate genome compaction such as histone tail modifications that change electrostatic interactions. Multiscale modelling of nucleosomes and chromatin fibres, following the present approach requires development of a corresponding CG model describing histones and their interactions. The model shall take into account important hydrophobic and hydrogen bonding effects, which can be difficult to describe within such CG models and that may require the combination with trained top-down approaches for parameterisation. Hence, this is still a major step to be accomplished but our present work along those lines shows that such an extension may be feasible (A. Mirzoev *et al.*, unpublished). Finally, in order to rigorously evaluate the time dynamics in the mesoscale simulations, generalised Langevin dynamics with friction parameters extracted from underlying detailed simulations can be

performed, which enables the study of time-dependent condensation behaviour (67,68).

DATA AVAILABILITY

All data needed to evaluate the conclusions in the paper are present in the paper and/or the Supplementary Data. Additional data related to this paper may be requested from the authors.

SUPPLEMENTARY DATA

Supplementary Data are available at NAR Online.

ACKNOWLEDGEMENTS

We are indebted to Profs. Aatto Laaksonen and Francesca Mocci for discussions and suggestions. We acknowledge the generous support of computer time allocation from the National Supercomputing Centre (NSCC) Singapore.

FUNDING

Singapore Ministry of Education Academic Research Fund (AcRF) Tier 2 [MOE2014-T2-1-123 (ARC51/14)] and Tier 3 [MOE2012-T3-1-001] to L.N.; Swedish Research Council [2017-03950] to A.P.L.. Funding for open access charge: Nanyang Technological University.
Conflict of interest statement. None declared.

REFERENCES

1. Bloomfield,V.A. (1997) DNA condensation by multivalent cations. *Biopolymers*, **44**, 269–282.
2. Gelbart,W.M., Bruinsma,R.F., Pincus,P.A. and Parsegian,V.A. (2000) DNA-inspired electrostatics. *Phys. Today*, **53**, 38–44.
3. Thomas,T.J. and Thomas,T. (2018) Collapse of DNA in packaging and cellular transport. *Int. J. Biol. Macromol.*, **109**, 36–48.
4. Carrivain,P., Cournac,A., Lavelle,C., Lesne,A., Mozziconacci,J., Paillusson,F., Signon,L., Victor,J.M. and Barbi,M. (2012) Electrostatics of DNA compaction in viruses, bacteria and eukaryotes: functional insights and evolutionary perspective. *Soft Matter*, **8**, 9285–9301.
5. Ausió,J., González-Romero,R. and Woodcock,C.L. (2014) Comparative structure of vertebrate sperm chromatin. *J. Struct. Biol.*, **188**, 142–155.
6. Hud,N.V. and Downing,K.H. (2001) Cryoelectron microscopy of lambda phage DNA condensates in vitreous ice: the fine structure of DNA toroids. *Proc. Natl. Acad. Sci. U.S.A.*, **98**, 14925–14930.
7. Joyeux,M. (2015) Compaction of bacterial genomic DNA: clarifying the concepts. *J. Phys. Condens. Matter*, **27**, 383001.
8. Livolant,F. (1991) Ordered phases of DNA in vivo and in vitro. *Physica A*, **176**, 117–137.
9. Wong,J.T.Y. (2019) Architectural organization of dinoflagellate liquid crystalline chromosomes. *Microorganisms*, **7**, 27.
10. Strom,A.R., Emelyanov,A.V., Mir,M., Fyodorov,D.V., Darzacq,X. and Karpen,G.H. (2017) Phase separation drives heterochromatin domain formation. *Nature*, **547**, 241–245.
11. Larson,A.G., Elnatan,D., Keenen,M.M., Trnka,M.J., Johnston,J.B., Burlingame,A.L., Agard,D.A., Redding,S. and Narlikar,G.J. (2017) Liquid droplet formation by HP1α suggests a role for phase separation in heterochromatin. *Nature*, **547**, 236–240.
12. Gao,X., Kim,K.-S. and Liu,D. (2007) Nonviral gene delivery: what we know and what is next. *AAPS J.*, **9**, E92–E104.
13. Evdokimov,Y.M., Platonov,A.L., Tikhonenko,A.S. and Varshavsky,Y.M. (1972) A compact form of double-stranded DNA in solution. *FEBS Lett.*, **23**, 180–184.
14. Laemmli,U.K. (1975) Characterization of DNA condensates induced by poly(ethylene oxide) and polylysine. *Proc. Natl. Acad. Sci. U.S.A.*, **72**, 4288–4292.
15. Gosule,L.C. and Schellman,J.A. (1976) Compact form of DNA induced by spermidine. *Nature*, **259**, 333-335.
16. Chattoraj,D.K., Gosule,L.C. and Schellman,J.A. (1978) DNA condensation with polyamines: II. Electron microscopic studies. *J. Mol. Biol.*, **121**, 327–337.
17. Wilson,R.W. and Bloomfield,V.A. (1979) Counterion-induced condensation of deoxyribonucleic acid. A light-scattering study. *Biochemistry*, **18**, 2192–2196.
18. Sikorav,J.L., Pelta,J. and Livolant,F. (1994) A liquid crystalline phase in spermidine-condensed DNA. *Biophys. J.*, **67**, 1387–1392.
19. Pelta,J., Livolant,F. and Sikorav,J.L. (1996) DNA aggregation induced by polyamines and cobalthexamine. *J. Biol. Chem.*, **271**, 5656–5662.
20. Nakata,M., Zanchetta,G., Chapman,B.D., Jones,C.D., Cross,J.O., Pindak,R., Bellini,T. and Clark,N.A. (2007) End-to-end stacking and liquid crystal condensation of 6 to 20 base pair DNA duplexes. *Science*, **318**, 1276–1279.
21. Conwell,C.C., Vilfan,I.D. and Hud,N.V. (2003) Controlling the size of nanoscale toroidal DNA condensates with static curvature and ionic strength. *Proc. Natl. Acad. Sci. U.S.A.*, **100**, 9296–9301.
22. Hud,N.V. and Vilfan,I.D. (2005) Toroidal DNA condensates: unraveling the fine structure and the role of nucleation in determining size. *Annu. Rev. Biophys. Biomol. Struct.*, **34**, 295–318.
23. Klimenko,S.M., Tikchonenko,T.I. and Andreev,V.M. (1967) Packing of DNA in the head of bacteriophage T2. *J. Mol. Biol.*, **23**, 523–533.
24. Leforestier,A. and Livolant,F. (2009) Structure of toroidal DNA collapsed inside the phage capsid. *Proc. Natl. Acad. Sci. U.S.A.*, **106**, 9157–9162.
25. Schellman,J.A. and Parthasarathy,N. (1984) X-ray diffraction studies on cation-collapsed DNA. *J. Mol. Biol.*, **175**, 313–329.
26. Brewer,L.R. (2011) Deciphering the structure of DNA toroids. *Integr. Biol. (Camb).*, **3**, 540–547.
27. Korolev,N., Lyubartsev,A.P. and Nordenskiöld,L. (2010) Cation-induced polyelectrolyte-polyelectrolyte attraction in solutions of DNA and nucleosome core particles. *Adv. Colloid Interface Sci.*, **158**, 32–47.
28. Podgornik,R. and Licer,M. (2006) Polyelectrolyte bridging interactions between charged macromolecules. *Curr. Opin. Colloid Interface Sci.*, **11**, 273–279.
29. Kang,H., Yoo,J., Sohn,B.-K., Lee,S.-W., Lee,H.S., Ma,W., Kee,J.-M., Aksimentiev,A. and Kim,H. (2018) Sequence-dependent DNA condensation as a driving force of DNA phase separation. *Nucleic Acids Res.*, **46**, 9401–9413.
30. Yoo,J. and Aksimentiev,A. (2016) The structure and intermolecular forces of DNA condensates. *Nucleic Acids Res.*, **44**, 2036–2046.
31. Stevens,M.J. (1999) Bundle binding in polyelectrolyte solutions. *Phys. Rev. Lett.*, **82**, 101–104.
32. Stevens,M.J. (2001) Simple simulations of DNA condensation. *Biophys. J.*, **80**, 130–139.
33. Ou,Z. and Muthukumar,M. (2005) Langevin dynamics of semiflexible polyelectrolytes: Rod-toroid–globule-coil structures and counterion distribution. *J. Chem. Phys.*, **123**, 074905.
34. Dey,A. and Reddy,G. (2017) Toroidal condensates by semiflexible polymer chains: Insights into nucleation, growth and packing defects. *J. Phys. Chem. B*, **121**, 9291–9301.
35. Ishida,H. and Kono,H. (2017) H4 tails potentially produce the diversity in the orientation of two nucleosomes. *Biophys. J.*, **113**, 978–990.
36. Yoo,J. and Aksimentiev,A. (2012) Improved parametrization of Li^+, Na^+, K^+, and Mg^{2+} ions for all-atom Molecular Dynamics simulations of nucleic acid systems. *J. Phys. Chem. Lett.*, **3**, 45–50.
37. Dans,P.D., Walther,J., Gomez,H. and Orozco,M. (2016) Multiscale simulation of DNA. *Curr. Opin. Struct. Biol.*, **37**, 29–45.
38. Takada,S. (2012) Coarse-grained molecular simulations of large biomolecules. *Curr. Opin. Struct. Biol.*, **22**, 130–137.
39. Dans,P.D., Zeida,A., MacHado,M.R. and Pantano,S. (2010) A coarse grained model for atomic-detailed DNA simulations with explicit electrostatics. *J. Chem. Theory Comput.*, **6**, 1711–1725.
40. Snodin,B.E., Randisi,F., Mosayebi,M., Šulc,P., Schreck,J.S., Romano,F., Ouldridge,T.E., Tsukanov,R., Nir,E., Louis,A.A. *et al.* (2015) Introducing improved structural properties and salt

dependence into a coarse-grained model of DNA. *J. Chem. Phys.*, **142**, 234901.
41. Hinckley,D.M. and de Pablo,J.J. (2015) Coarse-Grained ions for nucleic acid modeling. *J. Chem. Theory Comput.*, **11**, 5436–5446.
42. Savelyev,A. and Papoian,G.A. (2010) Chemically accurate coarse graining of double-stranded DNA. *Proc. Natl. Acad. Sci. U.S.A.*, **107**, 20340–20345.
43. Coronel,L., Micheletti,C. and Suma,A. (2018) Dynamics of supercoiled DNA with complex knots: large-scale rearrangements and persistent multi-strand interlocking. *Nucleic Acids Res.*, **46**, 7533–7541.
44. Brandner,A., Schüller,A., Melo,F. and Pantano,S. (2018) Exploring DNA dynamics within oligonucleosomes with coarse-grained simulations: SIRAH force field extension for protein-DNA complexes. *Biochem. Biophys. Res. Commun.*, **498**, 319–326.
45. Henrich,O., Gutiérrez Fosado,Y.A., Curk,T. and Ouldridge,T.E. (2018) Coarse-grained simulation of DNA using LAMMPS: An implementation of the oxDNA model and its applications. *Eur. Phys. J. E Soft Matter*, **41**, 57.
46. de Pablo,J.J. (2011) Coarse-grained simulations of macromolecules: from DNA to nanocomposites. *Annu. Rev. Phys. Chem.*, **62**, 555–574.
47. Hinckley,D.M., Freeman,G.S., Whitmer,J.K. and de Pablo,J.J. (2013) An experimentally-informed coarse-grained 3-site-per-nucleotide model of DNA: Structure, thermodynamics, and dynamics of hybridization. *J. Chem. Phys.*, **139**, 144903.
48. Córdoba,A., Hinckley,D.M., Lequieu,J. and de Pablo,J.J. (2017) A molecular view of the dynamics of dsDNA packing inside viral capsids in the presence of ions. *Biophys. J.*, **112**, 1302–1315.
49. Lyubartsev,A.P., Mirzoev,A., Chen,L.-J. and Laaksonen,A. (2010) Systematic coarse-graining of molecular models by the Newton inversion method. *Faraday Discuss.*, **144**, 43–56.
50. Mirzoev,A., Nordenskiöld,L. and Lyubartsev,A. (2019) Magic v.3: An integrated software package for systematic structure-based coarse-graining. *Comput. Phys. Commun.*, **237**, 263–273.
51. Sun,T., Mirzoev,A., Korolev,N., Lyubartsev,A.P. and Nordenskiöld,L. (2017) All-atom MD simulation of DNA condensation using ab initio derived force field parameters of cobalt(III)-hexammine. *J. Phys. Chem. B*, **121**, 7761–7770.
52. Fan,Y., Korolev,N., Lyubartsev,A.P. and Nordenskiöld,L. (2013) An advanced coarse-grained nucleosome core particle model for computer simulations of nucleosome-nucleosome interactions under varying ionic conditions. *PLoS One*, **8**, e54228.
53. Korolev,N., Di,L., Lyubartsev,A.P. and Nordenskiöld,L. (2014) A coarse-grained DNA model parametrized from atomistic simulations by Inverse Monte Carlo. *Polymers*, **6**, 1655–1675.
54. Mirzoev,A.A. and Lyubartsev,A.P. (2011) Effective solvent-mediated interaction potentials of Na^+ and Cl^- in aqueous solution: temperature dependence. *Phys. Chem. Chem. Phys.*, **13**, 5722–5727.
55. Mirzoev,A. and Lyubartsev,A.P. (2013) MagiC: Software package for multiscale modeling. *J. Chem. Theory Comput.*, **9**, 1512–1520.
56. Plimpton,S. (1995) Fast parallel algorithms for short-range molecular dynamics. *J. Comp. Phys.*, **117**, 1–19.
57. Baumann,C.G., Smith,S.B., Bloomfield,V.A. and Bustamante,C. (1997) Ionic effects on the elasticity of single DNA molecules. *Proc. Natl. Acad. Sci. U.S.A.*, **94**, 6185–6190.
58. Porschke,D. (1991) Persistence length and bending dynamics of DNA from electrooptical measurements at high salt concentrations. *Biophys. Chem.*, **40**, 169–279.
59. Cairney,K.L. and Harrington,R.E. (1982) Flow birefringence of T7 phage DNA: dependence on salt concentration. *Biopolymers*, **21**, 923–934.
60. Hagerman,P.J. (1988) Flexibility of DNA. *Annu. Rev. Biophys. Biophys. Chem.*, **17**, 265–286.
61. Kam,Z., Borochov,N. and Eisenberg,H. (1981) Dependence of laser light scattering of DNA on NaCl concentration. *Biopolymers*, **20**, 2671–2690.
62. Rizzo,V. and Schellman,J. (1981) Flow dichroism of T7 DNA as a function of salt concentration. *Biopolymers*, **20**, 2143–2163.
63. Manning,G.S. (1981) A procedure for extracting persistence lengths from light-scattering data on intermediate molecular weight DNA. *Biopolymers*, **20**, 1751–1755.
64. Naômé,A., Laaksonen,A. and Vercauteren,D.P. (2014) A solvent-mediated coarse-grained model of DNA derived with the systematic Newtion inversion method. *J. Chem. Theory Comput.*, **10**, 3541–3549.
65. Korolev,N., Berezhnoy,N.V., Eom,K.D., Tam,J.P. and Nordenskiöld,L. (2012) A universal description for the experimental behavior of salt-(in)dependent oligocation-induced DNA condensation. *Nucleic Acids Res.*, **40**, 2808–2821.
66. Yoo,J. and Aksimentiev,A. (2018) New tricks for old dogs: improving the accuracy of biomolecular force fields by pair-specific corrections to non-bonded interactions. *Phys. Chem. Chem. Phys.*, **20**, 8432–8449.
67. Hijón,C., Español,P., Vanden-Eijnden,E. and Delgado-Buscalioni,R. (2010) Mori-Zwanzig formalism as a practical computational tool. *Faraday Discuss.*, **144**, 301–322.
68. Lei,H., Caswell,B. and Karniadakis,G.E. (2010) Direct construction of mesoscopic models from microscopic simulations. *Phys. Rev. E.*, **81**, 026704.